Separating Double-Beta Decay Events from Solar Neutrino Interactions in a Kiloton-Scale Liquid Scintillator Detector

Andrey Elagin[a,*], Henry J. Frisch[a], Brian Naranjo[b], Jonathan Ouellet[c], Lindley Winslow[c], Taritree Wongjirad[c]

[a] *Enrico Fermi Institute, University of Chicago, Chicago, IL, 60637*
[b] *University of California, Los Angeles, CA, 90024*
[c] *Massachusetts Institute of Technology, Cambridge, MA 02139*
[d] *Nuclear Science Division, Lawrence Berkeley National Laboratory, Berkeley, CA 94720*

Abstract

We present a technique for separating double beta decay ($\beta\beta$-decay) events from background due to ^{8}B solar neutrino interactions. This background becomes dominant in a kilo-ton scale liquid scintillator detector. In searches for the neutrinoless double beta decay ($0\nu\beta\beta$-decay) ^{8}B background is usually considered as irreducible due to an overlap in the energy deposition. We note that in a liquid scintillator detector electrons from $0\nu\beta\beta$-decay often exceed Cherenkov threshold. Selection of early photons using fast photo-detectors separates prompt directional Cherenkov light from delayed isotropic scintillation light. This leads to the possibility of reconstructing the event topology of $0\nu\beta\beta$-decay candidate events by analyzing spatial distribution of early photons. Using a simulation of a 6.5 m radius liquid scintillator detector with 100 ps resolution photo-detectors, we perform a spherical harmonics analysis of the early light emitted in each candidate event and show the difference between $0\nu\beta\beta$-decay signal and ^{8}B background events. We discuss key detector parameters that affect the separation power.

*Corresponding Author: `elagin@hep.uchicago.edu`

Contents

1. Introduction

Over the past decade and a half, neutrino oscillation experiments have been able to conclusively establish that neutrinos have mass [1–4]. However, the nature of that mass remains one of the most fundamental open questions in particle physics. Is the neutrino unique among the Standard Model fermions with a Majorana mass [5], as is predicted by most beyond the standard model (BSM) theories, or does it have a Dirac-type mass like the rest of the fermions? A Majorana-type mass would have far reaching implications, from explaining the lightness of the neutrino and providing a bridge to higher energy phenomena through the see-saw mechanism [6, 7] to being able to provide the required lepton-number violation (LNV) and CP-violation needed for leptogenesis to explain the baryon asymmetry of the universe [8, 9]. Conversely, a Dirac neutrino mass could point to an underlying symmetry of the Universe.

Presently, the most promising technique for answering these questions is the search for Neutrinoless Double-Beta ($0\nu\beta\beta$) decay [10]. In this decay, a nucleus undergoes a second order β-decay without producing any neutrinos, $(Z, A) \rightarrow (Z + 2, A) + 2\beta^-$. This is in contrast to two-neutrino double beta ($2\nu\beta\beta$) decay [11], the second order Standard Model β-decay channel in which lepton number is conserved by the production of two anti-neutrinos, $(Z, A) \rightarrow (Z, A + 2) + 2\beta + 2\bar{\nu}_e$.

Liquid scintillator-based detectors have proven to be a competitive technology in this search[12]. Their primary advantage is their ease of scalability to larger instrumented masses, which involves dissolving larger amounts of the isotope of interest into the liquid scintillator (LS). This feature can allow for rapid scaling to 1 ton or more using the detectors already in operation [13]. In a large LS detector, most backgrounds can be strongly suppressed through a combination of filtration of the LS to remove internal contaminants, self-shielding to minimize the effects of external contaminants, and vetoes to reduce muon spallation backgrounds. The backgrounds relevant to $0\nu\beta\beta$ decay which cannot be reduced through these means are the $2\nu\beta\beta$ decay, electron scattering of ^{8}B solar neutrinos.

3

The $0\nu\beta\beta$ signal and these backgrounds have distinctive energy spectra. Since $0\nu\beta\beta$ decay produces no neutrinos, the full energy of the decay is contained within the detector and a peak is observed around the decay Q-value. This defines a region of interest (ROI) around the Q-value. In $2\nu\beta\beta$ decay, the neutrinos carry away some fraction of the decay energy leading to a broad spectrum of deposited energy from 0 MeV up to the decay Q-value. The interaction of ^{8}B solar neutrinos through neutrino-electron elastic scattering (ES) produces a spectrum that rises at low energies, producing an effectively flat background in the ROI [14].

A detector with good energy resolution can statistically separate these backgrounds from the $0\nu\beta\beta$ signal. Additional background rejection is possible with the inclusion of directional or topographical information. The two electrons emitted in $0\nu\beta\beta$ and $2\nu\beta\beta$ should reconstruct very differently from the single electron from ^{8}B events. In previous work, we have shown that photo-detectors with timing resolution of ~100 ps can be used to resolve the prompt Cherenkov photons from the slower scintillation signal and the resulting distributions can be fit for the position and direction of ~MeV electrons[15].

In this paper, we examine in detail the time and topographical distributions of $0\nu\beta\beta$-decay signal and ^{8}Bbackground. We propose a method using spherical harmonic decomposition to analyze the distribution of early photo-electrons (PE) and use this as a discriminant. In Section 2, we describe the detector model we will use throughout this paper. Details on event kinematics and PE timing for signal and background are given in Section 3 In Section 4, we introduce the spherical harmonic decomposition, and discuss the performance of this analysis in Section 5.

2. Detector Model

The same simulation using Geant4 version 4.9.6 as in Ref. [15] is used to model a sphere of 6.5 m radius filled with liquid scintillator. We consequently limit our discussion of the simulation to a summary of the most relevant parameters.

4

The scintillator composition has been chosen to match a KamLAND-like scintillator[2]. The composition is 80%

n-dodecane, 20% pseudocumene and 1.52 g/l PPO with a density of ρ = 0.78 g/ml). We use the Geant4 default

liquid scintillator optical model, in which optical photons are assigned the group velocity in the wavelength region of

normal dispersion. Wavelength dependent attenuation length[18], scintillation emission spectrum[18], and refractive

index[19] are used. The scintillator light yield is assumed to be 9030 photons/MeV) with Birks quenching ($kB \approx$

0.1 mm/MeV)[20]. However, we do deviate from the baseline KamLAND case in that the re-emission of absorbed

photons in the scintillator bulk volume and optical scattering, specifically Rayleigh scattering, have not yet been

included. A test simulation shows that the effect of optical scattering is negligible [15].

In this study, we use the fact that scintillators have inherent time constants that slow this light relative to the

Cherenkov light with wavelengths too long to be absorbed by the scintillator, between 360-370 nm for this scintillator.

The key inputs to the simulation are thus the time constants inherent to the scintillator cocktail that will determine the

timing of the scintillation light relative to the unperterbed Cherenkov light. The first step in the scintillation process

is the transfer of the energy deposited by the primary particles from the scintillator's solvent to the solute. The time

constant of this energy transfer accounts for a rise time in scintillation light emission. Because past neutrino exper-

iments were not highly sensitive to the effect of the scintillation rise time, there is a lack of accurate measurements

of this property. We assume a rise time of 1.0 ns from a re-analysis of the data in Ref. [21] but more detailed studies

are needed. The decay time constants are determined by the vibrational energy levels of the solute and are measured

to be τ_{d1} = 6.9 ns and τ_{d2} = 8.8 ns with relative weights of 0.87 and 0.13 for the KamLAND scintillator [22]. In a

detector of this size, chromatic dispersion, red light travelling faster than blue due to the wave-length dependent index

of refraction, enhances the separation but is not the dominant effect.

The inner sphere surface is used as the photodetector. It is treated as fully absorbing, no reflections, with 100%

photocathode coverage. As in the case of optical scattering, reflections at the sphere are a small effect that would create a small tail at longer times. The quantum efficiency (QE) of a bialkali photocathode (Hamamatsu R7081 PMT)[23], see also Ref. [24]. We note that the KamLAND 17-inch PMTs use the same photocathode type with similar quantum efficiency. In order to neglect the effect of the transit-time-spread (TTS) of the photodetectors, we use a TTS of 0.1 ns (σ), which can be achieved with large area picosecond photodetectors (LAPPDs)[25–32]. We neglect any threshold effects in the photodetector readout electronics and the photoelectron hit positions and the detection times after the TTS resolution has been applied are used for event reconstruction.

3. Kinematics and Timing of Signal and Background events

3.1. 0νββ-decay signal and 2νββ-decay background

In both 0νββ-decay signal and 2νββ-decay background events near the decay energy spectrum endpoint, the kinematics of the electron pair is very similar. Large fraction of events have a nearly back-to-back topology with a close to equal energy split between electrons. To simulate 0νββ- and 2νββ-decay events we use a Monte Carlo generator based on phase factors from Ref. [**?**]. Similarity in kinematics of 0νββ- and 2νββ-decay events is demonstrated in Fig. 1.

The electron angular correlations for 0νββ-decay are noticeably different from 2νββ-decay due to a contribution from the neutrino wave-functions even at vanishingly small energies of the neutrinos [**?**]. However, any practical use of this difference in separating 0νββ-decay from 2νββ-decay would require extremely large number of candidate events. Given the half-time of 2νββ-decay and upper limits on the half-time of 0νββ-decay, electron angular correlations will not bring a decisive separation power in controlling 2νββ-decay background in currently planned 0νββ-decay experiments. Excellent energy resolution at the Q-value remains the key parameter in 2νββ background suppression.

While we do not exclude that the angular correlations as an input to a multivariative technique may improve sensitivity of 0νββ-decay searches, in this paper we assume that there is no difference in the event topology between 0νββ- and 2νββ-decay events. Any conclusions about 0νββ-decay events also hold for 2νββ-decay when the total energy of the electrons in 2νββ-decay events is close to the Q-value.

Examining the kinematics for one of the 0νββ electrons with equal energy split, a 1.26 MeV electron travels a total path length of 0.X cm, has a distance from the origin of 0.X cm in 0.0X±0.00X ns and takes 0.0X±0.00X ns to drop below Cherenkov threshold. We note that due to scattering of the electron, the final direction of the electron before
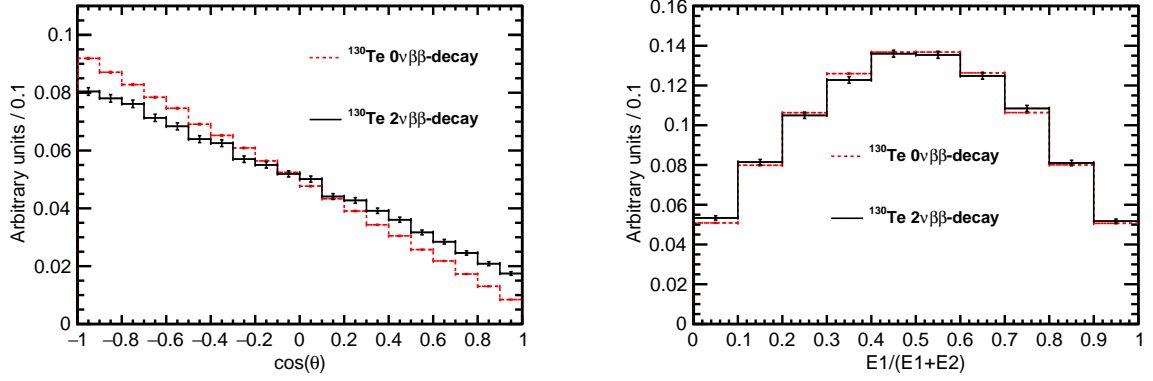
7

Figure 1: Comparison between kinematics of $0\nu\beta\beta$ (*dashed red lines*) and $2\nu\beta\beta$ decays (*solid black lines*) for events with the total kinetic energy of the electrons above 90% of the Q-value. *Left:* Cosine of the angle between two electrons. *Right:* Fraction of energy carried by one of the two electrons. Vertical bars at each bin of the histograms indicate statistical uncertainty for that bin.

it stops does not correspond to the initial direction; however the scattering angle is small at the time the majority of

Cherenkov light is produced.

Figure 2 shows the output of the detector simulation for 1000 simulated ^{130}Te $0\nu\beta\beta$-decay events. The left-hand

panel in Fig. 2 compares PE arrival time between Cherenkov and scintillation light. The right-hand panel shows the

composition of the early PE sample, which is key to direction and topographical reconstruction, selected with the

time cut of 33.5 ns. Each ^{130}Te $0\nu\beta\beta$-decay produces total of 6X±X PEs in the early PE sample. There are 3X±X

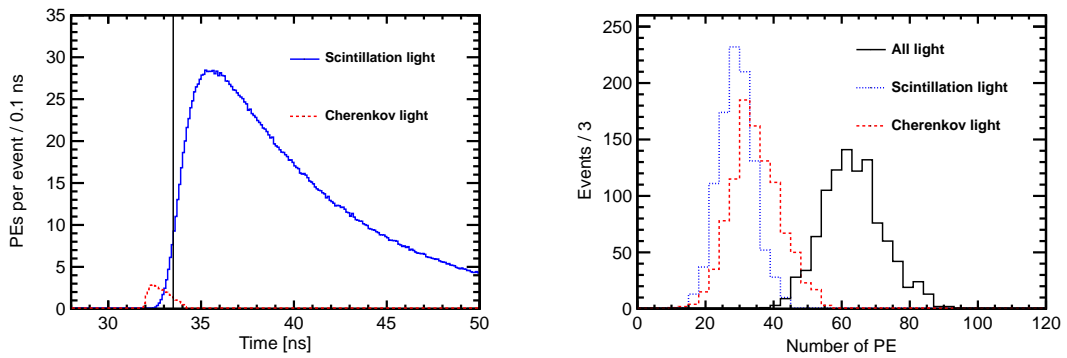scintillation and 3X±X Cherenkov PEs.

Figure 2: *Left:* Photo-electron (PE) arrival times after application of the photo-detector transit time spread (TTS) of 100 ps for the default simulation of ^{130}Te $0\nu\beta\beta$-decay produced at the center of the detector. Scintillation PEs (blue solid line) are compared to Cherenkov PEs (red dotted line) The vertical line at 33.5 ns indicates the time cut for the selection of the early PE sample. *Right:* Composition of the early PE sample: number of Cherenkov (*dashed red line*), scintillation (*dotted blue line*), and total (*solid black line*) PEs per event.

8

¹³⁴ Selection of PEs with relatively small arrival time allows the selection of a sample of PEs with a high fraction

¹³⁵ of directional Cherenkov light. This allows for event topology reconstruction. In particular, signal-like events with

¹³⁶ exactly two electrons can be separated from events with only one electron such as from ^{8}B solar neutrino interactions.

¹³⁷ *3.2. ^{8}B background*

¹³⁸ For a detector similar to our model, ^{8}B background is significant due to large total mass of the liquid scintillator

¹³⁹ in the active region of the detector. Electrons from elastic scattering of ^{8}B solar neutrinos have nearly a flat energy

¹⁴⁰ spectrum around the Q-value [14]. We simulate ^{8}B background as a single monochromatic electron with energy of

¹⁴¹ 2.53 MeV (Q-value of ^{130}Te). A 2.53 MeV electron travels a total path length of 0.X cm, has a distance from the

¹⁴² origin of 0.X cm in 0.0X±0.00X ns and takes 0.0X±0.00X ns to drop below Cherenkov threshold.

¹⁴³ The shape of scintillation and Cherenkov PE timing distributions in ^{8}B events match very closely the shape of

¹⁴⁴ corresponding distributions for 0$\nu\beta\beta$-decay events shown in Fig. 2. The electron path length is too short compared to

¹⁴⁵ the detector size to introduce any noticable difference in the shape of PE timing distributions between a single electron

¹⁴⁶ from ^{8}B events and two electrons from 0$\nu\beta\beta$-events.

¹⁴⁷ Each ^{8}B event produces total of 7X±X PEs in the early PE sample. There are 3X±X scintillation and 4X±X

¹⁴⁸ Cherenkov PEs. The total energy depositited in the detector in ^{8}B and 0$\nu\beta\beta$-decay events is the same. This leads to

¹⁴⁹ the same amount of scintillation light produced in the detector. The number of Cherenkov photons is slightly higher

¹⁵⁰ for ^{8}B events because the Cherenkov light is being produced by a single electron with the same kinetic energy as the

¹⁵¹ sum of kinetic energy of two electrons in 0$\nu\beta\beta$-decay events.

¹⁵² We do note use small difference in the total number of PEs in the early PE sample to separate 0$\nu\beta\beta$-decay signal

¹⁵³ from ^{8}B background. However, it may provide an extra handle on signal-background separation in a multivariative

¹⁵⁴ analysis when combined with directional and topographical information.

4. Event Topology and Spherical Harmonics Analysis

In this section we provide details about a spherical harmonics analysis to separate $0\nu\beta\beta$-decay signal events from ^{8}B background. We show that a spherical harmonics decomposition of the PE hits on the detector surface is sensitive to the differences between two-electron ($0\nu\beta\beta$-decay events) and single-electron (^{8}B events) topologies.

4.1. Topology of $0\nu\beta\beta$-decay and ^{8}B Events

When a typical $0\nu\beta\beta$-decay candidate isotope is considered, all ^{8}B background events will have the single electron above Cherenkov threshold in a liquid scintillator. Also a large fraction of $0\nu\beta\beta$-decay signal events will have both electrons above Cherenkov threshold. Cherenkov photons from each of the electrons will produce ring shaped clusters of PE hits on the detector surface. Therefore, any event reconstruction algorithm that is capable of separating events with one Cherenkov cluster from events with two Cherenkov clusters should have some signal-background discrimination power.

In some cases only one Cherenkov cluster is produced in $0\nu\beta\beta$-decay signal events. This happens either when the angle between the two $0\nu\beta\beta$-decay electrons is small and Cherenkov clusters overlap, or when the energy split between electrons is not balanced, causing one electron to be below Cherenkov threshold. Such signal events cannot be separated from background based on the topology of the Cherenkov photons distribution on the detector surface. However, directionality of the electron that is above Cherenkov threshold can still be reconstructed. This directionality information may allow for suppression of ^{8}B events based on the position of the sun.

Identification of the Cherenkov clusters is challenging due to much higher amount of uniformly distributed scintillation light that is produced in every event. We found that spherical harmonics analysis on an early PE sample which has a relatively high fraction of Cherenkov PE makes it possible to separate some **(quantify? this paragraph may belong to Sec.4 intro.)** of the $0\nu\beta\beta$-decay signal events from backgrounds.

4.2. Description of Spherical Harmonics Analysis

For the purpose of illustration of the spherical harmonics analysis concept we first consider three distinct topolo-

gies: two electrons produced back-to-back at an 180° angle, two electrons at a 90° angle, and a single electron.

Figure 3 shows an idealized simulation of these three topologies for a total electron energy of 10 MeV. In order to

emphasize ring patterns formed by Cherenkov photons the electron multiple scattering process is turned off in this

idealized simulation. Here the single-electron event represents an idealized ^{8}B event topology and the two-electron

events represent two special cases of an idealized $0\nu\beta\beta$-decay topology.

The central strategy of the spherical harmonics analysis is to construct rotationally invariant variables that can be

used to separate different event topologies. To this end, let the function $f(\theta, \phi)$ represent the PE distribution on the

detector surface. The function $f(\theta, \phi)$ can be decomposed into a sum of spherical harmonics:

$$f(\theta, \phi) = \sum_{l=0}^{\infty} \sum_{m=-l}^{l} f_{lm} Y_{lm}(\theta, \phi), \tag{1}$$

where Y_{lm} are Laplace's spherical harmonics defined in a real-value basis using Legendre polynomials P_l:

$$Y_{lm} = \begin{cases} \sqrt{2} N_{lm} P_l^m(cos\theta) cos\, m\phi, & \text{if } m > 0 \\[2ex] N_{lm} = \sqrt{\frac{(2l+1)}{4\pi} \frac{(l-m)!}{(l+m)!}}, & \text{if } m = 0 \\[2ex] \sqrt{2} N_{l|m|} P_l^{|m|}(cos\theta) sin\, |m|\phi, & \text{if } m < 0 \end{cases} \tag{2}$$

where the coefficients f_{lm} are defined as

$$f_{lm} = \int_0^{2\pi} d\phi \int_0^{\pi} d\theta sin\theta f(\theta, \phi) Y_{lm}(\theta, \phi). \tag{3}$$

11

Equation 4 defines the power spectrum of $f(\theta, \phi)$ in the spherical harmonics representation, s_l, where l is a multiple moment. The power spectrum, s_l, is invariant under rotation. It is unique to each of the functions $f_i(\theta, \phi)$, $i = 1, 2, 3...$, which can not be transformed into each other by rotation.

$$s_l = \sum_{m=-l}^{m=l} |f_{lm}|^2 \tag{4}$$

The event topology in a spherical detector determines the distribution of the PE's on the detector sphere, and, therefore, a set of s_l's. These values can serve as a quantitative figure of merit for different event topologies. The rotation invariance of s_l's ensures that this figure of merit does not depend on the orientation of the event with respect to the chosen coordinate frame.

Sum of s_l's over all multiple moments equals to the L2 norm of the function $f(\theta, \phi)$:

$$\sum_{l=0}^{\infty} s_l = \int_{\Omega} |f(\theta, \phi)|^2 d\Omega. \tag{5}$$

Therefore, the normalized power spectrum,

$$S_l = \frac{s_l}{\sum_{l=0}^{\infty} s_l} = \frac{s_l}{\int_{\Omega} |f(\theta, \phi)|^2 d\Omega}, \tag{6}$$

can be used to compare the shapes of various functions $f(\theta, \phi)$ with different normalization. As the total number of PEs detected on the detector sphere fluctuates from event to event we use the normalized power S_l.

Bottom panel in Fig. 3 compares the normalized power spectra for the three representative event topologies. The normalized power spectrum is different for all three event topologies. As expected, the largest difference is between

12

single track and back-to-back events.

In practice, at energies relevant to $0\nu\beta\beta$-decay Cherenkov rings become very fuzzy due to electron multiple scattering. In most cases ~1 MeV electrons produce randomly shaped clusters of Cherenkov photons around the direction of the electron track.

Examples of ^{130}Te $0\nu\beta\beta$ and ^{8}B events simulated at the center of the detector are shown in Fig. 4. ^{130}Te events are generated based on the phase factors described in [?]. ^{8}B events are implemented as monochromatic electrons with the initial direction along x-axis. Multiple scattering is now included. The default QE is applied. Figure 4 shows early PEs that pass 33.5 ns time cut.

In this more realistic example, the uniformly distributed scintillation light makes it more difficult to visually distinguish the event topology. The power spectra shown in the bottom pannel of Fig. 4 are different only at l=0 and l=1. We propose to use this difference to separate $0\nu\beta\beta$-decay signal from ^{8}B background events.

As shown in the middle row of Fig. 4, $0\nu\beta\beta$ events become indistinguishable from single-track events when the angle between the two electrons is small and two Cherenkov clusters overlap. Event topologies of $0\nu\beta\beta$ and ^{8}B events are also very similar when only one electron from $0\nu\beta\beta$ is above the Cherenkov threshold. Therefore spherical harmonics analysis is most efficient for events with large angular separation between the two electrons and when both electrons are above Cherenkov threshold.

Being able to distinguish between two-tracks and single-track events using the spherical analysis can allow further cuts to be made. For example, one might use absolute directional information to suppress single track events where the direction of the track is consistent with the location of a known background such as the sun. Once a single track topology is established, one can use a centroid method (see Ref. [?]) to reconstruct directionality of the track (or two degenerate tracks) in order to suppress events that are aligned with the direction of ^{8}B solar neutrinos.

4.3. Spherical Harmonics Analysis and Off-center Events

229   In general, the power spectrum S_l is rotation invariant for a given topology only if events originate in the center

230 of the detector. In order to compare spherical harmonics for events with verticies away from the center a coordinate

231 transformation for each photon hit is needed. The necessary transformation applied for each PE within an event is

232 illustrated in Fig. 5. The solid circle in Fig. 5 has a radius R and shows the actual detector boundaries. The dotted

233 circle shows a new sphere with the same radius R, which now has the event vertex in its center. The radius vector of

234 each PE is stretched or shortened to its intersection with this new sphere using the transformation, $\vec{r}_{PE} = \frac{\vec{a}}{|\vec{a}|} \cdot R$, where

235 $\vec{r}_{PE}$ is a new radius vector of a PE and $\vec{a} = \vec{r}_{PE} - \vec{r}_{vtx}$ with $\vec{r}_{PE}$ and $\vec{r}_{vtx}$ being radius vectors of the PE and the vertex in

236 the original coordinates, respectively.

237 *4.4. Implementation of the spherical harmonics analysis*

238   Numerical calculation of the power spectrum is implemented as follows. For each event, we create a 2-D his-

239 togram, θ vs ϕ, with the distribution of PEs on the detector surface. We then treat this histogram as a function $f(\theta, \phi)$

240 where the value of the function for any pair of θ and ϕ is equal to the number of PE in the histogram bin corresponding

241 to that pair.

242   Coefficients f_{lm} from Eq. 3 are calculated using a Monte Carlo integration technique. Variables S_l's are calculated

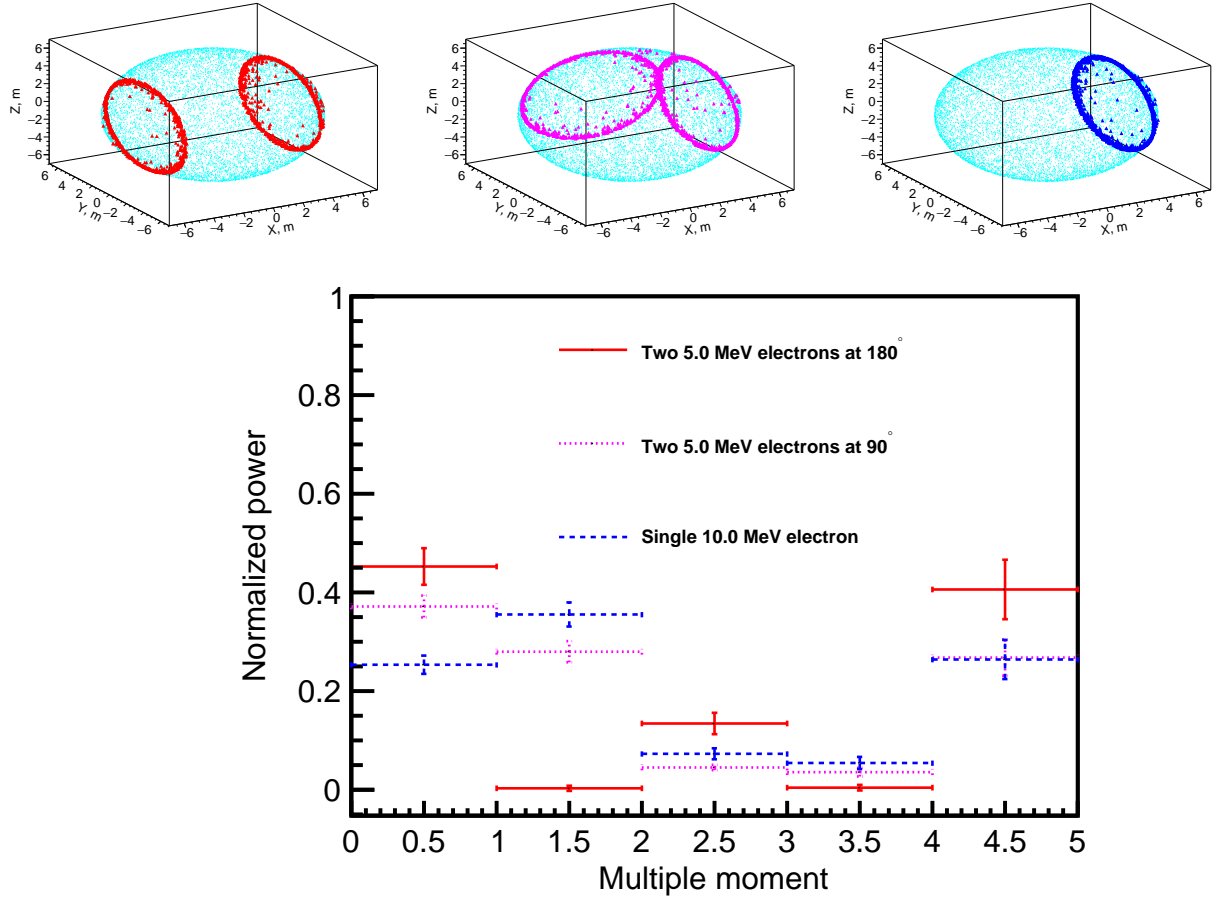243 using Eqs.4 - 6. **Also need to provide reference to the libraries for Legendre polynomials.**

Figure 3: *Top panels:* Idealized event displays for the three representative event topologies: two 5 MeV back-to-back electrons (*top left*), two 5 MeV electrons at 90° angle (*top middle*), and a single 10 MeV electron (*top right*). Multiple scattering is turned off in the simulation to emphasize the difference in the mutual orientation of Cherenkov rings for the three topologies. For the illustration purposes 100% QE is applied to Cherenkov photons (triangles) and the default QE is applied to scintillation photons (dots). All electrons originate at the center of the detector. One typical event is shown for each topology. *Bottom panel:* Normalized power spectrum S_l calculated for distribution of Cherenkov photons only. The three topologies are compared: two 5 MeV back-to-back electrons (*solid red line*), two 5 MeV electrons at 90° angle (*dotted magenta line*), and a single 10 MeV electron (*dashed blue line*). For each topology 100 events were simulated. The normalized power values S_l's were calculated for each individual event. The horizontal lines correspond to the mean values of S_l within each event topology. The vertical bars show one standard deviation from the mean value.
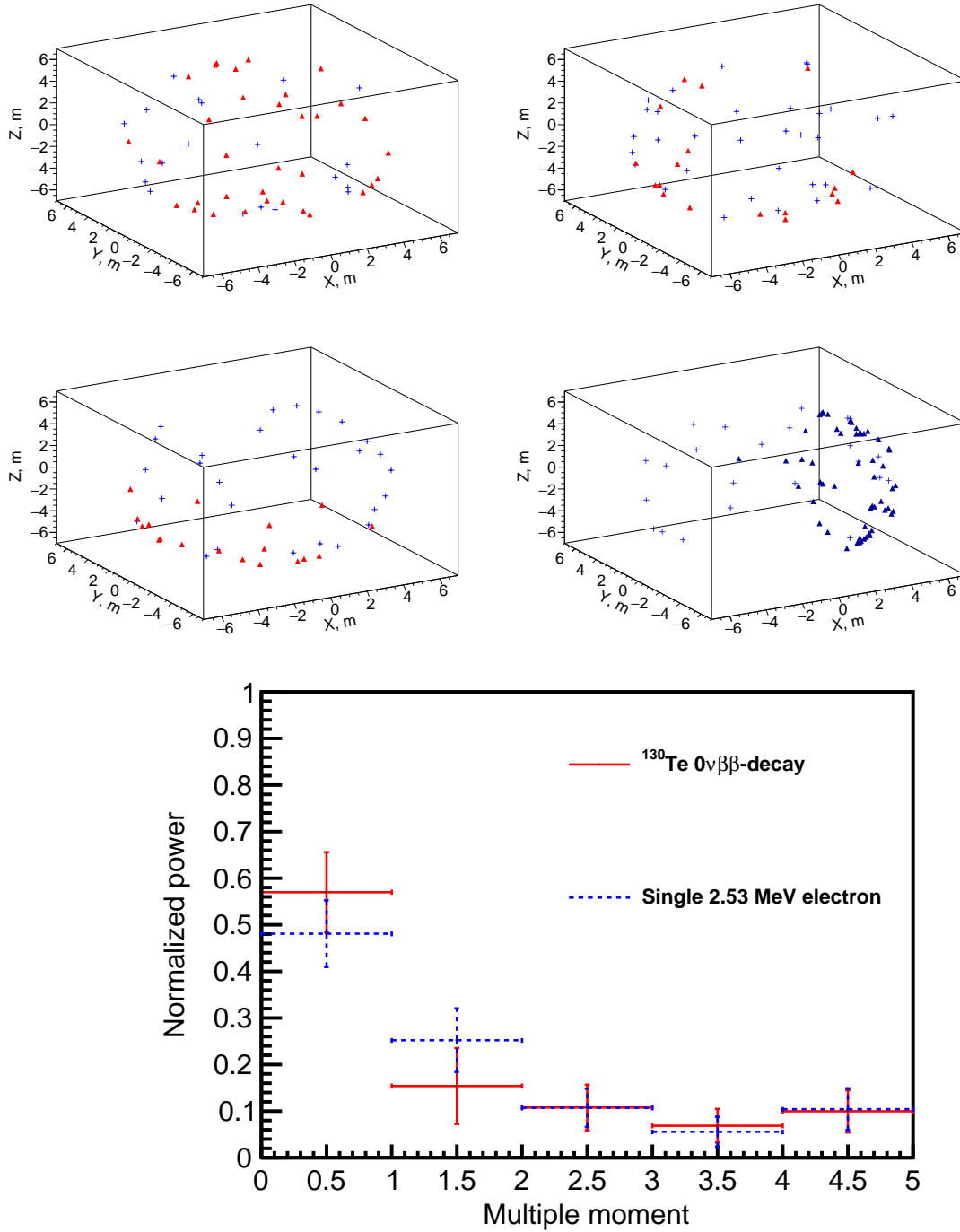
15

Figure 4: *Top and middle rows:* Event display examples for ^{130}Te $0\nu\beta\beta$-decay signal and ^{8}B background events. The default QE and the time cut of 33.5 ns are applied to both Cherenkov (*triangles*) and scintillation (*crosses*) photons. For the ^{130}Te $0\nu\beta\beta$-decay signal three representative events are shown each closely matching on of the three topologies. A typical single electron event is shown for the ^{8}B background. *Top left:* ^{130}Te $0\nu\beta\beta$-decay back-to-back electrons: E_1=1.257 MeV, E_2=1.270 MeV, cos(θ)=-0.908. *Top right:* ^{130}Te $0\nu\beta\beta$-decay electrons at ~90°: E_1=1.264 MeV, E_2=1.263 MeV, cos(θ)=-0.029. *Middle left:* ^{130}Te $0\nu\beta\beta$-decay electrons at ~0°: E_1=1.186 MeV, E_2=1.340 MeV, cos(θ)=0.888. *Middle right:* 2.529 MeV single electron. In all events electrons originate at the center of the detector. *Bottom panel:* Normalized power spectrum S_l calculated for distribution of all PE after the 33.5 ns time cut. ^{130}Te $0\nu\beta\beta$-decay signal (*solid red line*) and ^{8}B background (*dashed blue line*) topologies are compared. Simulation of 1000 signal and background events. The normalized power values S_l's were calculated for each individual event. The horizontal lines correspond to the mean values of S_l. The vertical bars show one standard deviation from the mean value.
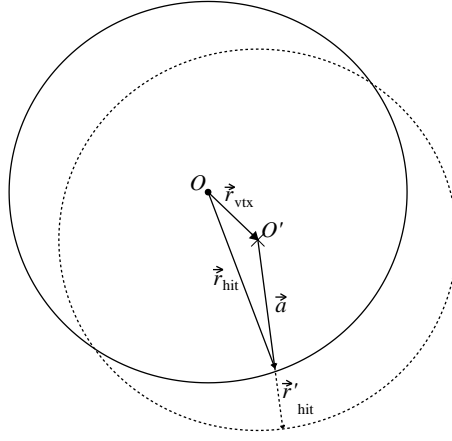
Figure 5: Coordinate transformation applied to events that are off-center. The solid circle schematically shows actual detector boundaries. The dotted circle shows a new sphere of radius R=6.5 m with the event vertex position in the center. The radius vector of each photon hit is stretched or shortened until the intersection with this new sphere using the transformation $\vec{r}'_{hit} = \frac{\vec{a}}{|\vec{a}|} \cdot R$. Where $\vec{r}'_{hit}$ is a new radius vector of the photon hit, R is detector sphere radius, and $\vec{a} = \vec{r}_{hit} - \vec{r}_{vtx}$ with $\vec{r}_{hit}$ and $\vec{r}_{vtx}$ being radius vectors of the photon hit and vertex position in original coordinates and correspondingly.

5. Performance of the Spherical Harmonics Analysis in Separating $0\nu\beta\beta$-decay from ^{8}B Background.

In this section we discuss factors that affect performance of the spherical harmonics analysis in separating $0\nu\beta\beta$ signal from ^{8}B background events. We found that most separation comes from the first two multiple moments, $l = 0$ and $l = 1$. However, according to Eq. 6, higher multiple moments are needed for a better normalization of the power spectrum S_l. In the following we choose to calculate the power spectrum s_l up to l=3 and use only normalized variable S_0 and S_1, where the normalization is given by

$$S_{0,1} = \frac{s_{0,1}}{\sum_{l=0}^{3} s_l} \tag{7}$$

As discussed below, a linear combination of S_0 and S_1 can be used to construct a single variable, S_{01}, that provides separation between signal and background in 1-D space. We show distributions of this variable S_{01} to demonstrate qualitatively the separation between $0\nu\beta\beta$ and ^{8}B events depending on a few key assumptions about the detector characteristics.

The following paragraph needs to be moved to intro and maybe re-phrased. *Since the goal of this paper is to describe the technique of spherical harmonics analysis for separating different event topologies relevant for $0\nu\beta\beta$-decay searches in a generic liquid scintillator detector, we intentionally refrain from any quantitative estimates on the improvements in sensitivity to $0\nu\beta\beta$ decay. The actual improvements in sensitivity due to spherical harmonics analysis would depend on various details of a given experimental setup. Therefore, we believe that detailed quantitative sensitivity studies are more appropriate in the context of a particular $0\nu\beta\beta$ decay experiment which is beyond the scope of this paper.*

5.1. Central events with no uncertainty on the vertex position

We start evaluating the performance of the spherical harmonics analysis by looking at events that originate at the center of the detector and by assuming perfect reconstruction of the event vertex position. For such events, a time cut of 33.5 ns on the PE arrival time can be applied to obtain early an PEs sample which contains a high fraction of Cherenkov PEs. The default QE and 100% photo-coverage are used in the simulation.

A comparison of S_0 and S_1 distributions for $0\nu\beta\beta$-decay signal and ^{8}B background events is shown in Fig. 6. Both variables provide a noticeable separation between signal and background. We also note that in the energy range of interest, the S_l's do not strongly depend on the energy deposited in the detector, which makes information contained in the normalized power spectrum complimentary to the energy measurements. Spherical harmonics analysis can thus be used as an additional handle for background suppression at the end point of the $0\nu\beta\beta$-decay energy spectrum.
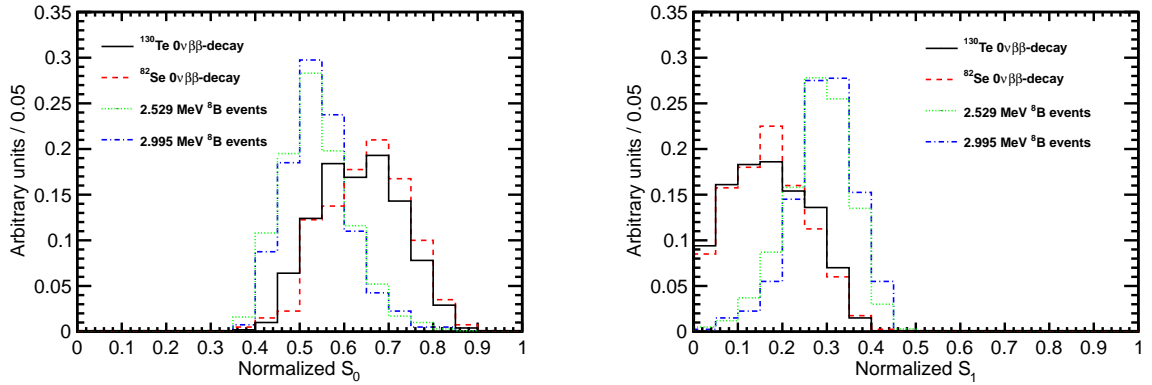

Figure 6: S_0 (*left*) and S_1 (*right*) distributions for 1000 simulated $0\nu\beta\beta$-decay signal and ^{8}B background events. Two different isotopes are compared, ^{130}Te and ^{82}Se. Corresponding kinetic energies of ^{8}B single electrons are 2.53 MeV and 3.00 MeV. Central events assuming perfect reconstruction of vertex position. Time cut of 33.5 ns on the PE arrival time is applied. The default QE and 100% photo-coverage is used in the simulation.

Left panel in Fig. 7 compares scatter plots of the first two components of the power spectrum, S_0 and S_1, for signal and background. In order to optimize separation between ^{130}Te and ^{8}B events, a linear combination of variables S_0 and S_1 is constructed as follows.

275 First, a linear fit, $S_0 = A \cdot S_1 + B$, of all points on the scatter plot is performed as shown by the dashed line in the left

276 panel in Fig. 7. Then a 1-D variable S_{01} is defined as $S_{01} = S_1 \cdot cos(\theta) + S_0 \cdot sin(\theta)$, where $tan(\theta)=A$. The right-hand

277 panel in Fig. 7 compares distributions of S_{01} for $0\nu\beta\beta$-decay signal and ^{8}B background. These 1-D histograms for

278 S_{01} represent the projection of the points on the scatter plot onto the fitted line. We use the distribution of the variable

279 S_{01} as a figure of merit for signal/background separation. Figure 7 demonstrates that spherical harmonics analysis

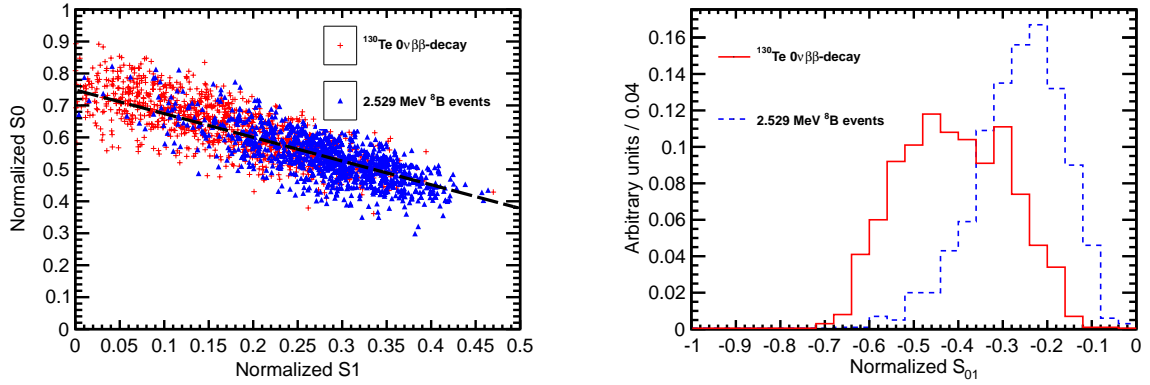280 potentially brings extra separation power which is in addition to the energy measurements.

Figure 7: *Left:* Scatter plot of S_0 versus S_1 for a simulation of 1000 signal (*red crosses*) and background (*blue triangles*) events. Central events assuming perfect reconstruction of vertex position. Time cut of 33.5 ns on the PE arrival time is applied. The default QE and 100% photo-coverage is used in the simulation. Black dashed line corresponds to a linear fit to define 1-D variable S_{01} (see text for details). *Right:* Comparison of the S_{01} distribution between signal (*red solid line*) and background (*blue dashed line*).

281 *5.2. Experimental challenges: chromatic dispersion and vertex resolution*

282 So far only events at the center of the detector have been considered. Precise vertex reconstruction has been also

283 assumed. Here we discuss performance of the spherical harmonics analysis for events that originate throughout the

284 whole fiducial volume of the detector and that also have limited vertex reconstruction precision.

285 Selection of the early PE sample using the absolute time cut of 33.5 ns that has been applied to central events relies

286 on the fact that, within the uncertainty on electron track length, all photons travel the same distance before reaching

287 the surface of the detector. PEs with early measured time correspond mostly to Cherenkov photons because of the

288 delay in the scintillation process and longer wavelength of the Cherenkov light.

20

Since in general the vertex is not at the center of the detector, a uniform absolute time cut on the photon arrival time is no longer effective in selecting Cherenkov photons. In the case of an off-center vertex, even significantly delayed scintillation photons can reach the side of the detector that is closer to the vertex much earlier than Cherenkov photons traveling to the opposite side of the detector. The time cut thus has to take into account the total distance traveled by each individual photon.

We found that a differential time cut defined as $\Delta t = t_{measured}^{phot} - t_{predicted}^{phot} < 1$ ns selects photons with a sufficient fraction being Cherenkov photons. However, when this differential time cut is applied, chromatic dispersion and vertex resolution significantly reduce the Cherenkov/scintillation light separation in the early PE sample. and therefore, reduce discrimination power of the spherical harmonics analysis. In the following we describe both effects and propose solutions to mitigate their influence on the spherical harmonics analysis.

The predicted time, $t_{predicted}^{phot} = l/v^{phot}$, depends on the distance, l, traveled by the photon and the velocity of the photon, v^{phot}. Since the wavelength information is not available for a given PE, we use an average index of refraction, n, and define the photon velocity as $v^{phot} = c/n$. This uncertainty on the photon velocity makes the differential time cut less effective in separating Cherenkov light from scintillation light.

Similarly to the effect of chromatic dispersion, the vertex uncertainty makes the differential time cut less efficient in separating Cherenkov and scintillation light. An uncertainty on the vertex position leads to an uncertainty on the photon predicted travel time, $t_{predicted}^{phot}$, which in turn increases the probability to mix scintillation and Cherenkov light in the early PE sample.

In addition, in the case of single electron event topology, a small error in vertex reconstruction could cause a large effect on the normalized power spectrum of spherical harmonics.

The early PE sample of the single electron topology typically has a strong asymmetry due to preferential direc-

21

tionality of Cherenkov PEs that are selected together with uniformly distributed scintillation PEs. A mis-reconstructed

vertex introduces an artificial asymmetry in the selection of scintillation PEs. Vertex shifts parallel to the direction of

the electron track have the largest effect compared to the shifts in the transverse direction.

If a vertex is shifted in the direction opposite to the track of the electron, the differential time cut selects more

scintillation photons that are emitted in the direction of the electron track. Therefore scintillation photons would

enhance forward asymmetry of the early PE sample, which in turn, would move S_1 to higher values[1].

If a vertex is shifted in the same direction as the direction of the electron, the differential time cut selects more

scintillation photons that are emitted in the direction opposite to the electron track. Therefore, the asymmetry of

Cherenkov PEs would be counter balanced by scintillation PEs, which in turn, would move S_1 to lower values.

5.3. Events in a fiducial volume with an uncertainty on the vertex position

We found that in our default detector model the separation power of the spherical harmonics analysis is reduced

to X when chromatic dispersion and vertex resolution are taken into account.

We simulated 1000 signal and background events that have their verticies uniformly distributed within a fiducial

volume of $R < 3$ m, where R is the distance between the event vertex and the center of the detector. To implement an

uncertainty on the vertex reconstruction we apply a 3 cm smearing around the actual vertex position for each simulated

event. The smearing is done along x, y, and z directions with three independent Gaussian distributions of the same

width, $\sigma_x = \sigma_y = \sigma_z = 3$ cm.

Figure 8 shows the performance of the spherical harmonics analysis under these more realistic assumptions. The

overlap of the S01 distributions between signal and background is Y%. The spherical harmonics analysis does not

bring any significant separation between signal and background in our default detector model after the chromatic

---

[1] In general, S_1 component of the spherical harmonics power spectrum is higher for asymmetric distributions and lower for symmetric distributions (e.g., compare back-to-back and single electron topologies in Fig. 3). Moreover, $S_1 = 0$ for a distribution with perfect symmetry with respect to the center of the sphere.

330 dispersion and vertex resolution are taken into account. However, properties of the liquid scintillator can be adjusted

331 to improve the performance of the spherical harmonics analysis. In the folowing we show that a single change in the

332 scintillation rise time restores most of the separation power that was shown previously in Fig. 7.
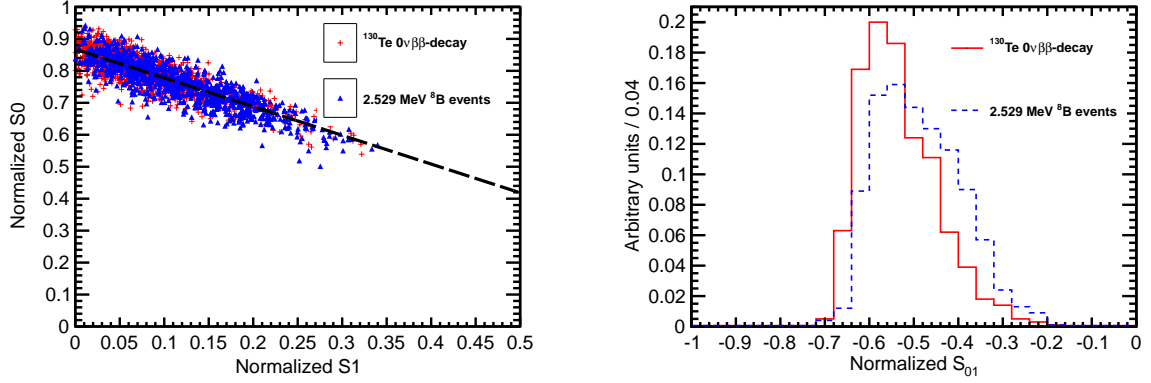

Figure 8: *Left:* Scatter plot of S_0 versus S_1 for a simulation of 1000 signal (*red crosses*) and background (*blue triangles*) events. Event verticies are uniformly distributed within the fiducial volume, $R < 3$ m. Vertex is smeared with 3 cm resolution. Differential cut of $\Delta t = t^{phot}_{measured} - t^{phot}_{predicted} < 1$ ns is applied to select early PE sample. The default QE and 100% photo-coverage is used in the simulation. Black dashed line corresponds to a linear fit to define 1-D variable S_{01} (see text for details). *Right:* Comparison of the S_{01} distribution between signal (*red solid line*) and background (*blue dashed line*).

5.4. Importance of the liquid scintillator properties

334 Strong dependence on the vertex resolution can be addressed by choosing a liquid scintillator mixture with a more

335 delayed emission of scintillation light with respect to Cherenkov light. With a larger delay in scintillation light, a

336 higher fraction of Cherenkov light can be maintained in the early PE sample even if a photon track length is mis-

337 reconstructed due to imprecise reconstruction of the vertex position. In addition, if the fraction of scintillation light is

338 small compared to Cherenkov light, the distortions in the uniformity of the scintillation PE due to shifted reconstructed

339 vertex position does not significantly affect spherical harmonics power spectrum.

340 While our default detector model assumes scintillation rise time of $\tau_r = 1$ ns, scintillation rise time up to $\tau_r = 7$ ns

341 can be achieved (see Ref. **??**). As a test we repeated spherical harmonics analysis on $0\nu\beta\beta$-decay and ^{8}B events after

342 increasing scintillation rise time parameter to $\tau_r = 5$ ns in our detector model. All other parameters are kept the same.

343 Figure 9 shows result of that test. The events are uniformly distributed within the fiducial volume and each vertex is

344 smeared with 3 cm resolution.

345 We conclude that a rise time of τ_r =5 ns provides sufficient delay between Cherenkov and scintillation light to

346 make spherical harmonics analysis a potentially useful technique to separate $0\nu\beta\beta$-decay signal from ^{8}B background.
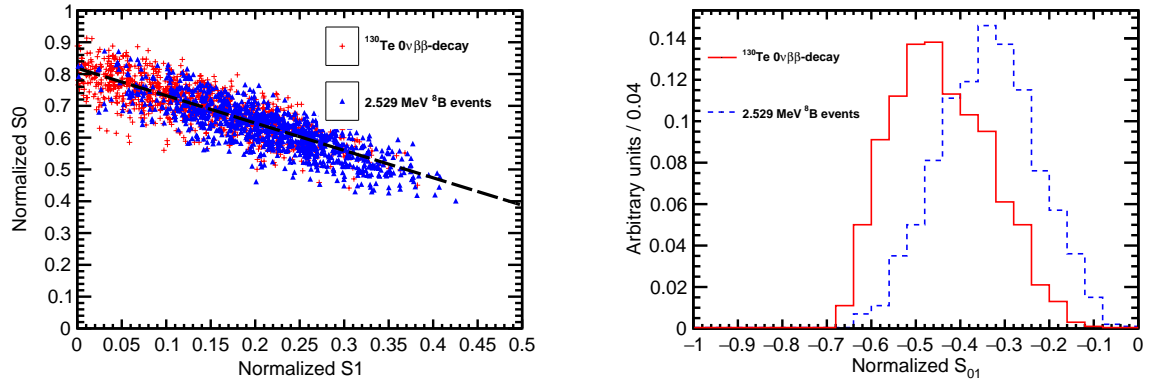

Figure 9: Scintillation rise time constant is increased to τ_r =5 ns compared to τ_r =1 ns in the default detector model. *Left:* Scatter plot of S_0 versus S_1 for a simulation of 1000 signal (*red crosses*) and background (*blue triangles*) events. Event verticies are uniformly distributed within the fiducial volume, $R < 3$ m. Vertex is smeared with 3 cm resolution. Differential cut of $\Delta t = t^{phot}_{measured} - t^{phot}_{predicted}$ <1 ns is applied to select early PE sample. The default QE and 100% photo-coverage is used in the simulation. Black dashed line corresponds to a linear fit to define 1-D variable S_{01} (see text for details). *Right:* Comparison of the S_{01} distribution between signal (*red solid line*) and background (*blue dashed line*).

347 Furthermore, the effects due to chromatic dispersion can be addressed by using liquid scintillators with a narrower

348 emission spectrum. For example, such as described in Ref. [**?**].

6. Conclusions

A technique based on spherical harmonics analysis can separate $0\nu\beta\beta$ decay from ^{8}B solar neutrino interactions. The separation is based on the distinct event topologies of signal and background. This event topology information is available in addition to the measurements of the energy deposited in the detector. This technique may be further developed and adopted by future large scale liquid scintillator detectors to suppress background coming from ^{8}B solar neutrino interactions in the detector volume. The performance of the technique is mostly affected by chromatic dispersion, vertex reconstruction and the time profile of the emission of scintillation light. We show that a liquid scintillator detector with a scintillation rise time constant τ_r =5 ns provide sufficient cherenkov-scintillation light separation and potentially allows for use of the spherical harmonics analysis as an extra handle to extract $0\nu\beta\beta$ decay signal.

Acknowledgements

References

[1] Q. R. Ahmad, et al., Phys. Rev. Lett. 87 (2001) 071301.
[2] K. Eguchi, et al., Phys. Rev. Lett. 90 (2003) 021802.
[3] Q. R. Ahmad, et al., Phys. Rev. Lett. 89 (2002) 011301.
[4] S. Fukuda, et al. (Super-Kamiokande), Phys. Lett. B 539 (2002) 179–187.
[5] E. Majorana, Nuovo Cim. 14 (1937) 171–184.
[6] M. Gell-Mann, P. Ramond, R. Slansky, Conf. Proc. C790927 (1979) 315–321.
[7] T. Yanagida, Proc. of the Workshop on Unified Theory and the Baryon Number of the Universe Japan (1979).
[8] M. Fukugita, T. Yanagida, Barygenesis without grand unification, Phys. Lett. B 174 (1986) 45 – 47.
[9] M. A. Luty, Phys. Rev. D 45 (1992) 455.
[10] W. H. Furry, Phys. Rev. 56 (1939) 1184–1193.
[11] M. Goeppert-Mayer, Phys. Rev. 48 (1935) 512–516.
[12] A. Gando, et al. (KamLAND-Zen), Phys. Rev. Lett. 110 (2013) 062502.
[13] S. D. Biller, Phys. Rev. D 87 (2013) 071301.
[14] A. Maio (SNO+), Search for Majorana neutrinos with the SNO+ detector at SNOLAB, J. Phys. Conf. Ser. 587 (2015) 012030.
[15] C. Aberle, A. Elagin, H. J. Frisch, M. Wetstein, L. Winslow, J. Instrum. 9 (2014) P06012.
[16] S. Agostinelli, et al. (GEANT4), GEANT4: A Simulation toolkit, Nucl. Instrum. Meth. A506 (2003) 250–303.
[17] J. Allison, et al., Geant4 developments and applications, Nuclear Science, IEEE Transactions on 53 (2006) 270–278.
[18] O. Tajima, *Development of Liquid Scintillator for a Large Size Neutrino Detector*, Master's thesis, Tohoku University, 2000.

392 [19] O. Perevozchikov, *Search for electron antineutrinos from the sun with KamLAND detector*, Ph.D. thesis, University of Tennessee, 2009.

393 [20] C. Grant, A Monte Carlo Approach to ^{7}Be Solar Neutrino Analysis with KamLAND, Ph.D. thesis, University of Alabama, 2012.

394 [21] C. Aberle, Optimization, simulation and analysis of the scintillation signals in the Double Chooz experiment, Ph.D. thesis, University of
395 Heidelberg, 2011.

396 [22] O. Tajima, *Measurement of Electron Anti-Neutrino Oscillation Parameters with a Large Volume Liquid Scintillator Detector, KamLAND*,
397 Ph.D. thesis, Tohoku University, 2003.

398 [23] Hamamatsu Photonics K.K., Large Photocathode Area Photomultiplier Tubes (data sheet, including R7081), 2013.
399 http://www.hamamatsu.com/resources/pdf/etd/LARGE_ AREA_PMT_TPMH1286E05.pdf.

400 [24] Y. Abe, et al. (Double Chooz), Reactor electron antineutrino disappearance in the Double Chooz experiment, Phys. Rev. D86 (2012) 052008.

401 [25] H. Grabas, R. Obaid, E. Oberla, H. Frisch, J.-F. Genat, R. Northrop, F. Tang, D. McGinnis, B. Adams, M. Wetstein, {RF} strip-line anodes
402 for psec large-area mcp-based photodetectors, Nucl.Instrum.Meth. A 711 (2013) 124 – 131.

403 [26] Oberla, E. and Genat, J. and Grabas, H. and Frisch, H. and Nishimura, K. and Varner, G., A 15 GSa/s, 1.5 GHz Bandwidth Waveform
404 Digitizing ASIC, Nucl.Instrum.Meth. A735 (2014) 452–461.

405 [27] B. Adams, et al., Invited article: A test-facility for large-area microchannel plate detector assemblies using a pulsed sub-picosecond laser,
406 Review of Scientific Instruments 84 (2013) 061301.

407 [28] B. Adams, et al., Measurements of the gain, time resolution, and spatial resolution of a 20x20cm^2 MCP-based picosecond photo-detector,
408 Nucl.Instrum.Meth. A732 (2013) 392–396.

409 [29] O. Seigmund, et al., Large area event counting detectors with high spatial and temporal resolution, J. Instrum. 9 (2014) C04002.

410 [30] B. Adams, et al., An internalALD-basedhighvoltagedividerandsignalcircuit for MCP-basedphotodetectors, Nucl.Instrum.Meth. A780 (2015)
411 107–113.

412 [31] B. Adams, et al., Timing characteristics of Large Area Picosecond Photodetectors, Nucl.Instrum.Meth. A795 (2015) 1–11.

413 [32] M. Minot, et al., Pilot production & commercialization of LAPPD^{TM}, Nucl.Instrum.Meth. A787 (2015) 78–84.